AGU PUBLICATIONS

Geophysical Research Letters

RESEARCH LETTER
10.1002/2015GL065727

Key Points:
- Iron supply is estimated using observations and a 3-D model of the Ross Sea
- The largest sources are winter mixing from the benthos and melting sea ice
- Inferred supply is sufficient to balance satellite-based productivity estimates

Supporting Information:
- Supporting Information S1

Correspondence to:
D. J. McGillicuddy,
dmcgillicuddy@whoi.edu

Citation:
McGillicuddy, D. J., Jr., et al. (2015), Iron supply and demand in an Antarctic shelf ecosystem, *Geophys. Res. Lett.*, *42*, doi:10.1002/2015GL065727.

Received 14 AUG 2015
Accepted 15 SEP 2015
Accepted article online 22 SEP 2015

Iron supply and demand in an Antarctic shelf ecosystem

D. J. McGillicuddy Jr.[1], P. N. Sedwick[2], M. S. Dinniman[2], K. R. Arrigo[3], T. S. Bibby[4], B. J. W. Greenan[5], E. E. Hofmann[2], J. M. Klinck[2], W. O. Smith Jr.[6], S. L. Mack[2], C. M. Marsay[2,7], B. M. Sohst[2], and G. L. van Dijken[3]

[1]Woods Hole Oceanographic Institution, Woods Hole, Massachusetts, USA, [2]Department of Ocean, Earth and Atmospheric Sciences, Old Dominion University, Norfolk, Virginia, USA, [3]Department of Earth System Science, Stanford University, Stanford, California, USA, [4]Ocean and Earth Science, National Oceanography Centre Southampton, University of Southampton, Southampton, UK, [5]Ocean and Ecosystem Sciences Division, Bedford Institute of Oceanography, Department of Fisheries and Oceans, Dartmouth, Nova Scotia, Canada, [6]Virginia Institute of Marine Science, College of William and Mary, Gloucester Point, Virginia, USA, [7]Now at Skidaway Institute of Oceanography, University of Georgia, Savannah, Georgia, USA

Abstract The Ross Sea sustains a rich ecosystem and is the most productive sector of the Southern Ocean. Most of this production occurs within a polynya during the November–February period, when the availability of dissolved iron (dFe) is thought to exert the major control on phytoplankton growth. Here we combine new data on the distribution of dFe, high-resolution model simulations of ice melt and regional circulation, and satellite-based estimates of primary production to quantify iron supply and demand over the Ross Sea continental shelf. Our analysis suggests that the largest sources of dFe to the euphotic zone are wintertime mixing and melting sea ice, with a lesser input from intrusions of Circumpolar Deep Water and a small amount from melting glacial ice. Together these sources are in approximate balance with the annual biological dFe demand inferred from satellite-based productivity algorithms, although both the supply and demand estimates have large uncertainties.

1. Introduction

Previous field and modeling studies [*Boyd et al*., 2012; *Fitzwater et al*., 2000; *Measures et al*., 2012; *Raiswell et al*., 2006; *Sedwick et al*., 2011] have identified a number of potential sources of dissolved iron to surface waters on Antarctic continental shelves. These include the vertical resupply of iron by winter convective mixing, shallow benthic inputs from banks and shoals, intrusions of Circumpolar Deep Water (CDW), and meltwater from sea ice and glacial ice, all of which are likely to be sensitive to climatic change. Hence, in regions such as the Ross Sea, where iron supply is thought to regulate primary production [*Arrigo et al*., 2003; *Martin et al*., 1990; *Sedwick et al*., 2000], an understanding of the relative importance of these sources is required to predict the ecological and biogeochemical impacts of a varying climate.

To quantify iron supply from these various sources, we conducted a detailed survey of the Ross Sea in austral summer 2011–2012, spanning key geographic locations and water masses (Figure 1). The primary inflows into the Ross Sea consist of Low-Salinity Shelf Water (LSSW) from the east and both CDW and Antarctic Surface Water (AASW) from offshore [*Jacobs and Giulivi*, 1999]. CDW mixes with ambient shelf water to become Modified Circumpolar Deep Water (MCDW). Brine rejection during sea ice formation leads to production of High-Salinity Shelf Water (HSSW). Ice Shelf Water (ISW) is created by cooling of waters in contact with the underside of the Ross Ice Shelf (RIS) at depth, leading to outflows from beneath the RIS with temperatures below the surface freezing point.

2. Methods

We combine observations and models to estimate iron supply (four distinct sources) and demand. Iron supply due to convective mixing is derived from homogenizing our observed iron profiles down to the maximum mixed layer depths simulated by our hydrodynamic model. Sources from MCDW, sea ice, and glacial ice are quantified with passive tracer simulations using observations to define the end-member concentrations. Iron demand is calculated from a satellite-based productivity algorithm, assuming an *f* ratio

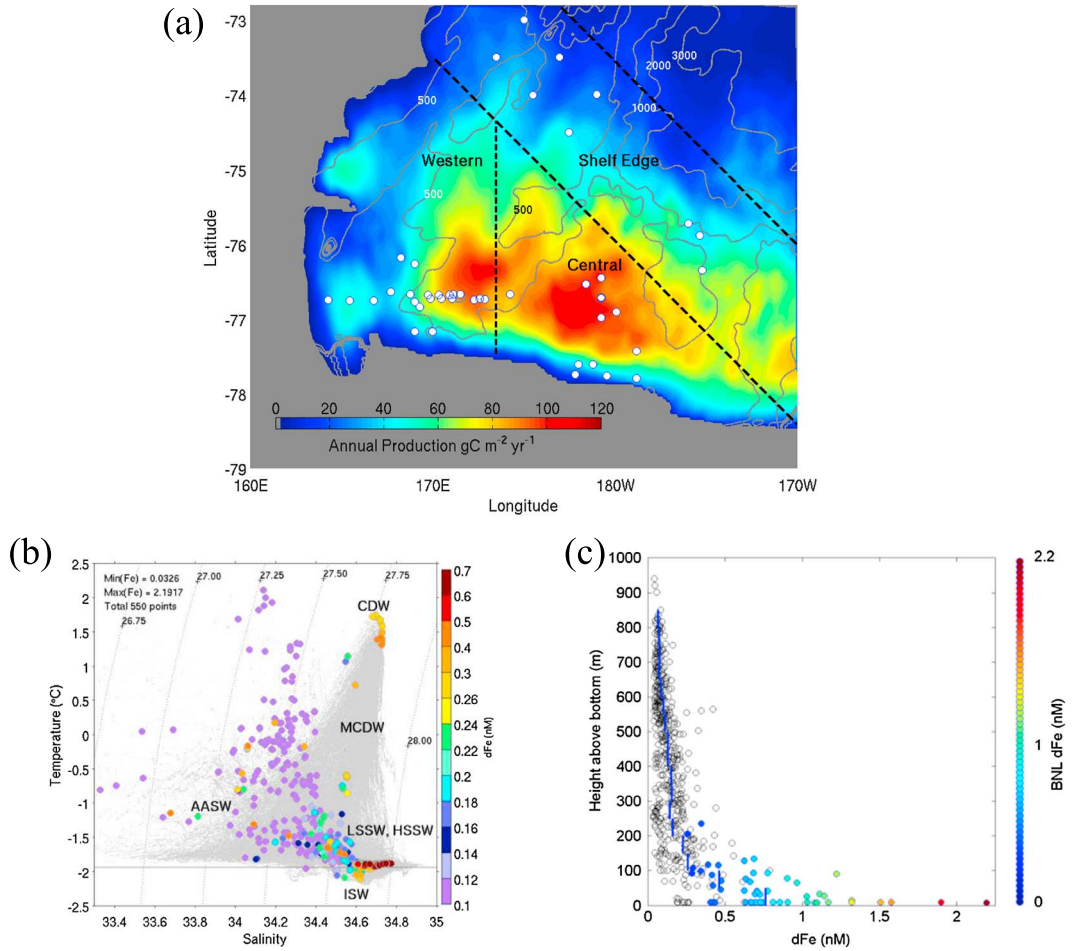

Figure 1. (a) Sampling locations in the western, central, and shelf edge subregions of the Ross Sea (boundaries for in situ and satellite data analysis depicted by dashed lines), overlaid on a satellite-derived estimate for mean annual production 1997–2013 (color shading coincident with the maximum ice-free area during that period; permanent ice cover is not distinguished from land in the gray mask). Seagoing observations (white dots) were collected in January–February 2012. (b) Observations of dFe (all depths) plotted as a function of temperature and salinity. Gray dots are all prior measurements from the World Ocean Database 2009 CTD data (see http://www.nodc.noaa.gov/OC5/SELECT/dbsearch/dbsearch.html), 140–230°E, 65–80°S, bottom depths < 2000 m, similar to the area selected in a recent climatology [*Orsi and Wiederwohl*, 2009]. Density contours (σ_T) are shown as dotted lines, and the freezing point of seawater at surface pressure and salinity of 35 is depicted as a horizontal solid line. See text for definitions of water masses indicated in bold. (c) Dissolved iron plotted as a function of height above bottom. Values are filled in color for those samples that occur within benthic nepheloid layers (BNLs) identified in transmissometer data for each station (Figure S1 in the supporting information). Blue bars indicate the mean iron concentration for each 50 m depth bin.

based on prior studies. This approach also requires phytoplankton carbon:iron uptake stoichiometry, for which values reported in the literature vary widely. Therefore, we use our data to constrain the drawdown ratio by computing the difference between our summertime observations and estimated wintertime concentrations of iron and nitrate, converting to carbon units with the Redfield ratio.

2.1. Seagoing Observations

Data were collected on voyage NBP1201 of the RVIB *Nathaniel B. Palmer*, 24 December 2011 to 8 February 2012. Hydrography and water samples were obtained using a rosette sampler fitted with 24 10-L Niskin bottles, together with conductivity, temperature, and depth (CTD) sensors and a transmissometer. Nitrate and other macronutrient concentrations were measured at sea using standard autoanalyzer techniques. Seawater samples for trace metal analysis were collected with custom-modified 5-L Teflon-lined external-closure Niskin-X samplers (General Oceanics) on a trace metal clean rosette deployed on a nonmetallic line, and dissolved iron (dFe) was determined postcruise following the methods described by *Sedwick et al*. [2011].

2.2. Tracer Transport Modeling

Ross Sea circulation and tracer transport was simulated with the Regional Ocean Modeling System (ROMS; http://www.myroms.org). The model domain extends from north of the shelf break (67.5°S) southward to 85°S and includes almost the entire cavity beneath the RIS. The horizontal grid spacing is 5 km, and there are 24 vertical levels. This model expands upon earlier simulations of the Ross Sea [*Dinniman et al*., 2011] with the inclusion of tidal forcing as well as a dynamic sea ice component. The simulation covers the time period 15 September 2010 to 27 February 2012, which includes the time period of observations examined here. The model is forced with European Centre for Medium-Range Weather Forecasts Interim winds and atmospheric temperatures. Lateral open boundary conditions are provided by climatology.

Three passive tracers were added to the model to estimate dFe fluxes from MCDW, melting sea ice, and meltwater from the base of floating glacial ice (predominantly the RIS). Circulation under the ice is represented, so dFe delivered from those areas to ice-free waters is included in supply estimates. A simple scavenging model is used to account for dFe removal by sinking particles along the transport pathways. Cumulative supply of new dFe is estimated from the simulated concentration in the euphotic zone at the end of the growing season, assuming complete utilization by phytoplankton.

Given the end-member concentrations of dFe and nitrate in each of the three water types, the simulated fluxes can be used to calculate the supply from each source. For MCDW, we use $dFe_{MCDW} = 0.27 \pm 0.05$ nM and $NO3_{MCDW} = 29.9 \pm 1.4$ μM based on our field measurements, which are consistent with prior observations in that water mass [*Sedwick et al*., 2011]. Nitrate in sea ice and glacial ice tends to be depleted relative to that in seawater, so nitrate supply from those sources is assumed to be negligible.

The concentration of dFe in Antarctic sea ice varies widely, with reported values ranging from 1 to 20 nM [*Lannuzel et al*., 2010]. The iron present in sea ice originates from both atmospheric deposition and the surrounding seawater, with the latter thought to predominate [*Lannuzel et al*., 2010]. Indeed, recent studies in McMurdo Sound concluded that iron in land-fast sea ice is derived primarily from the water column via sediment resuspension rather than aeolian sources [*de Jong et al*., 2013]; accumulation rates of aeolian iron on sea ice can account for only a small fraction of the new primary production in the southwestern Ross Sea [*Winton et al*., 2014]. A variety of mechanisms facilitate incorporation of waterborne iron into sea ice, including (1) direct inclusion of dFe through frazil and congelation ice growth, (2) incorporation of particulate and colloidal iron, and (3) colonization by microorganisms [*Lannuzel et al*., 2010]. In cases (2) and (3), additional processes are required to transform these various particulate forms into dFe. We used a median value of $dFe_{SeaIce} = 10 \pm 5$ nM, with the large uncertainty reflecting the variability in measured dFe concentrations in sea ice.

Unfortunately, we have no direct measurements of dFe in the glacial ice of the RIS. Glacial ice cores from the Talos Dome, about 250 km west of the Ross Sea, contain total iron concentrations ranging from 1.34 to 8.79 ng g^{-1} during the Holocene and Last Glacial Maximum, respectively [*Spolaor et al*., 2013]. Using these values, and assuming 32% solubility [*Edwards and Sedwick*, 2001], we estimate $dFe_{GlacialIce} = 29 \pm 21$ nM. *Death et al*. [2014] have suggested end-member dFe concentrations 2–3 orders of magnitude higher for subglacial meltwaters, but such values would cause the simulated glacial meltwater dFe concentrations to exceed the total dFe observed in waters adjacent to the RIS (Figure S10 in the supporting information). If the *Death et al*. [2014] end-members were applied only to the fraction of freshwater budget of the RIS cavity derived from the supply of subglacial meltwater across the grounding line (approximately 5% [*Carter and Fricker*, 2012]), our simulations suggest the overall glacial flux would contribute 50–500% of the observed concentrations in ISW. Obviously, the lower bound is possible, with the remaining 50% supplied by mixing from other sources such as MCDW. However, based on the present measurements, it is not possible to distinguish between subglacial and glacial meltwater.

The simulated fluxes associated with MCDW, sea ice, and glacial ice are used for two purposes: (1) to estimate the cumulative dFe and nitrate resupply at the space-time location of each station to facilitate drawdown calculations and (2) to compute annual dFe supply on both a subregional and shelf-wide basis. See supporting information for more details of the tracer transport calculations (including the dFe scavenging formulation), as well as quantitative evaluation of model skill based on available observations.

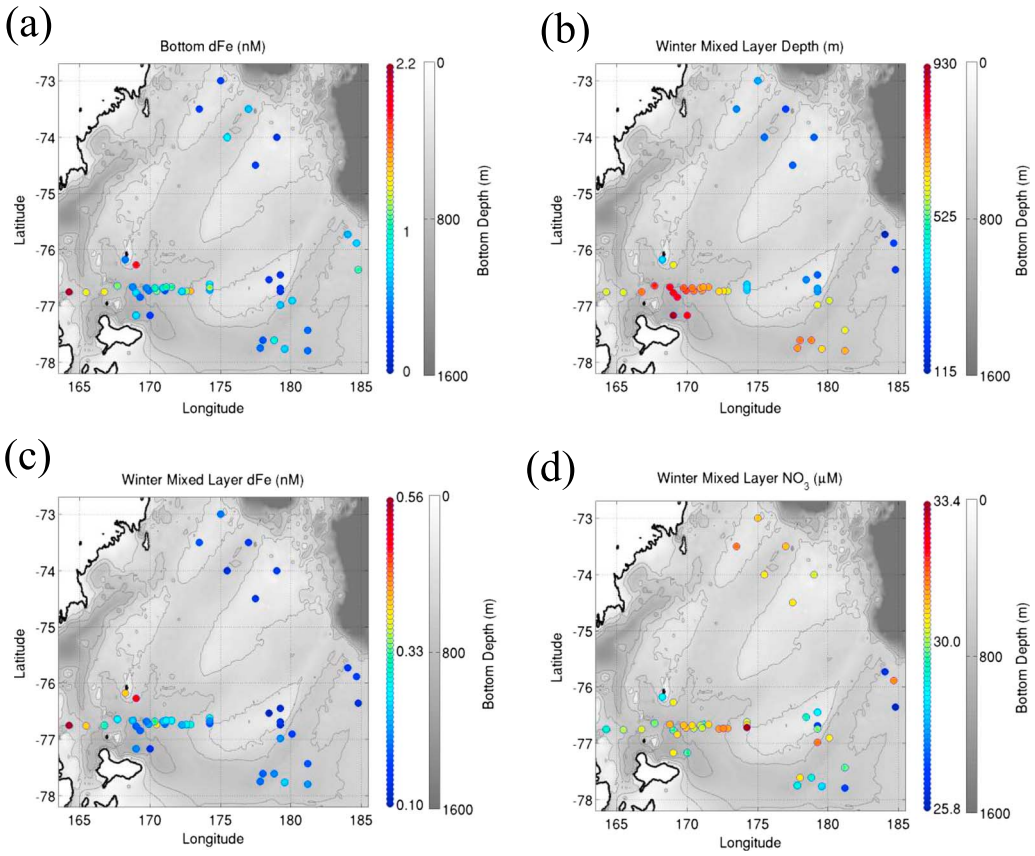

Figure 2. (a) Dissolved iron concentration in the deepest sample for each cast (colored dots). Bathymetry shaded in gray with contours at 200 m intervals. (b) Maximum mixed layer depth diagnosed from a ROMS hindcast. Note that the station near 177°49′E, 77°45′S is located underneath the Ross Ice Shelf in the model simulation, so its maximum mixed layer depth was taken to be that of the closest model grid point north of the ice shelf. Surface mixed layer (c) dissolved iron and (d) nitrate concentrations computed by homogenizing each profile to the depth of maximum mixing.

2.3. Satellite-Based Estimates of Net Primary Production

Daily maps of net primary production (NPP) for the Ross Sea were produced from satellite-derived chlorophyll *a* (Chl *a*), sea surface temperature, and sea ice cover using an algorithm developed for the Southern Ocean that explicitly includes light limitation [*Arrigo et al.*, 2008]. More details on the methods are provided in the supporting information. Briefly, the algorithm is tuned to match in situ NPP observations [*Arrigo et al.*, 2008], so the NPP estimates are not sensitive to the suspected bias in satellite chlorophyll *a* retrievals in the Southern Ocean. The algorithm assumes a fixed C:Chl *a* ratio in phytoplankton and therefore does not account for variations in this ratio associated with species composition, irradiance, and other environmental variables. In particular, the C:Chl *a* ratio has been shown to increase with iron deficiency [*Sunda and Huntsman*, 1997], a factor that varies seasonally in this region. However, increasing iron limitation also decreases phytoplankton growth, which would tend to compensate for increasing C:Chl *a* in terms of NPP.

Satellites can only detect Chl *a* in open waters, so phytoplankton within and beneath ice are not included in production estimates. Primary production within the ice itself, although locally important as a food source for zooplankton and krill, is a small fraction of total productivity in such regions [*Arrigo et al.*, 1997]. As for production in the water column beneath ice, prior observations suggest that little chlorophyll is present in those waters. For example, a section through ice-covered waters near Terra Nova Bay [*Arrigo et al.*, 2000] revealed reduced surface salinity (their Plate 2), low Chl *a* (their Plate 4B), and relatively little nitrate drawdown (their Plate 4C). Therefore, neglect of NPP within/beneath ice and its associated iron demand is not likely to constitute a large error in this analysis.

Table 1. Iron Supply and Demand for the Ross Sea and Regional Subdomains Shown in Figure 1a[a]

Inventories	All	Western	Central	Shelf Edge
Winter Fe (nM)	0.23 ± 0.10	0.29 ± 0.11	0.18 ± 0.05	0.15 ± 0.02
Winter NO_3 (μM)	30.0 ± 1.4	30.3 ± 0.7	29.6 ± 1.6	29.8 ± 2.0
NO_3:Fe drawdown 10^5 mol N /mol Fe	0.59 ± 0.22	0.54 ± 0.20	0.72 ± 0.22	0.42 ± 0.04
Nov–Feb Mean Mixed Layer Depth (m)				
	24.8	22.2	27.6	24.9
Fe Sources (μmol Fe m^{-2} yr^{-1})				
Drawdown of winter reserve	3.2 ± 2.5	4.2 ± 2.4	2.2 ± 1.4	1.2 ± 0.5
MCDW	1.3 ± 0.2	1.4 ± 0.3	1.9 ± 0.3	1.6 ± 0.3
Sea ice	3.1 ± 1.6	5.8 ± 2.9	1.9 ± 1.0	3.0 ± 1.5
Glacial ice	0.17 ± 0.12	0.33 ± 0.24	0.34 ± 0.25	0.04 ± 0.03
Sum	7.8 ± 4.4	11.8 ± 5.9	6.3 ± 2.9	5.9 ± 2.3
Fe Demand (μmol Fe m^{-2} yr^{-1})				
Satellite-based NP	8.8 ± 6.4	8.5 ± 6.2	9.9 ± 7.1	6.6 ± 4.8
Difference				
	1.0 ± 10.8	−3.2 ± 12.0	3.5 ± 10.1	0.6 ± 7.1

[a]Winter iron and nitrate concentrations estimated from cruise data and ROMS hindcast mixed layer depths. Drawdown ratios are computed assuming cumulative inputs of iron and nitrate from MCDW, sea ice, and glacial ice simulated for the space-time location of each station. Iron sources for the mixed layer are calculated from drawdown of the winter reserve and cumulative seasonal inputs simulated for each domain. Mixed layer depths for the growing season (November–February) calculated from the climatology available at http://www7320.nrlssc.navy.mil/nmld/nmld.html. Iron demand estimated from a satellite-based algorithm for new production assuming an *f* ratio of 0.5 ± 0.1 and a C:Fe ratio inferred from the estimated NO_3:Fe drawdown and Redfield stoichiometry. The reported uncertainties also reflect interannual variability in NPP (Figure S4 in the supporting information).

2.4. Conceptual Framework for Interpreting Iron Supply and Demand

A mechanistic link between iron supply and demand stems from the fact that iron limits phytoplankton production in the Ross Sea [*Sedwick et al.*, 2011; *Tagliabue and Arrigo*, 2005]. If the estimated demand were larger than supply, that would suggest that either demand was overestimated or that one or more of the sources was underestimated. On the other hand, if demand were less than supply, then either iron would have accumulated in the surface layer, been transported off the shelf [*Tagliabue et al.*, 2009], or supply (demand) was overestimated (underestimated). Agreement of the two independent estimates to within their associated uncertainties suggests that a steady state model of iron supply and demand is appropriate. However, an important caveat stems from the multiple time scales involved in this analysis: whereas our in situ observations come from a single year, our estimates of iron supply involve multiyear processes such as transport of MCDW and glacial melt from within the RIS cavity. As such, we compare with a multiyear mean (1997–2013) of satellite-based productivity. Interannual variability in the balance between iron supply and demand remains an important issue that will require long-term in situ time series observations.

3. Results

Our observations show that dFe concentrations were generally low enough to limit phytoplankton growth (~0.1 nM) in surface waters of the polynya, whereas CDW and ISW end-members had higher concentrations of ~0.3 nM (Figure 1b). The highest dFe concentrations were observed near the seafloor, often in association with benthic nepheloid layers (Figures 1c, 2a, and S1) in waters deeper than 400 m [*Marsay et al.*, 2014]. Nearly 40% of the total water column dFe inventory was contained within 100 m of the seafloor (Figure S2a in the supporting information), suggesting that benthic sources play a major role in iron cycling on the Ross Sea shelf. This benthic dFe is likely a mixture of remineralized biogenic material exported from the euphotic zone and exogenous inputs of lithogenic iron from the seafloor and terrigenous sediments. Enrichment of dFe near the seafloor was observed in all three subregions examined during our cruise (Figure S2b; the rationale for western, central, and shelf edge domains is provided in the supporting information).

An important mechanism for supply of benthic dFe to the euphotic zone is regional-scale convective mixing in winter, which can extend to the seafloor in some areas of the Ross Sea shelf [*Gordon et al.*, 2000]. This

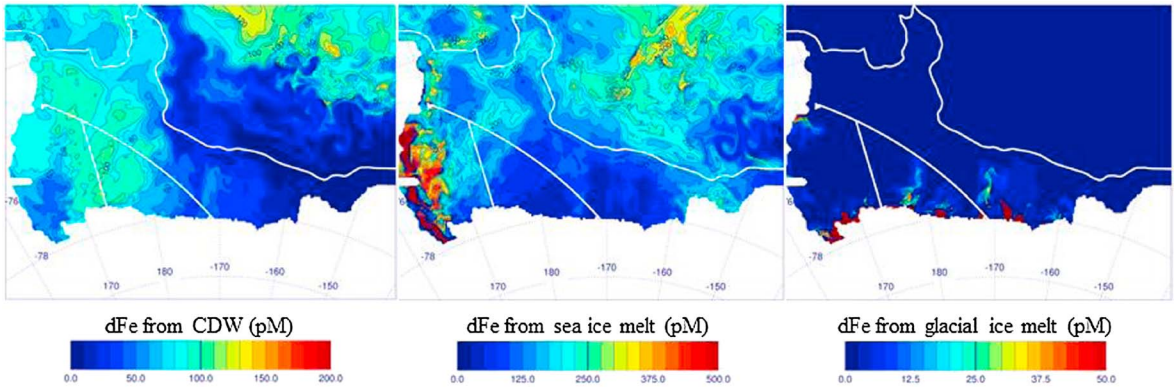

Figure 3. Model-derived estimates of dFe supplied to the upper mixed layer during the growing season due to intrusions of (left) CDW, (middle) melting sea ice, and (right) glacial meltwater. White lines show the boundaries between the three regional subdomains depicted in Figure 1: western, central, and shelf edge. Note that the offshore limit of the shelf edge domain is defined by the 1200 m isobath because the source of CDW in the tracer simulation was assumed to be seaward of that boundary. Note that the color scales are different in each panel.

mixing sets a "winter reserve" of dFe in surface waters at the start of the growing season. To quantify this, we extracted the depth of maximum mixing from the circulation model hindcast (Figure 2b). These mixing depths are sufficient to ventilate most of the water column over much of the area sampled during our cruise, with the exception of deeper areas near the shelf edge and some of the deeper troughs. Based on our summertime observations of dFe and nitrate profiles in the water column, and the hindcast maximum mixed layer depth for each station (MLD_i), winter concentrations for iron and nitrate are estimated as

$$\widehat{\mathrm{dFe}_i} = \frac{1}{\mathrm{MLD}_i}\int_{\mathrm{MLD}_i}^{0} \mathrm{dFe}(z)_i \, \mathrm{d}z$$

$$\widehat{\mathrm{NO3}_i} = \frac{1}{\mathrm{MLD}_i}\int_{\mathrm{MLD}_i}^{0} \mathrm{NO3}(z)_i \, \mathrm{d}z$$

with the coordinate z defined to be positive upward. Values of $\widehat{\mathrm{dFe}_i}$ range from 0.10 to 0.56 nM, whereas values of $\widehat{\mathrm{NO3}_i}$ range from 25.9 to 33.4 μM (Figures 2c and 2d). Wintertime observations with which to compare these predictions are scarce, but these ranges are not inconsistent with data from early spring [*Coale et al.*, 2005; *Sedwick et al.*, 2000], although the capacity for rapid utilization of the winter reserve of iron [*Sedwick et al.*, 2011] complicates this comparison. Interestingly, $\widehat{\mathrm{dFe}_i}$ in the western Ross Sea is significantly higher than in the other two regions considered, yet $\widehat{\mathrm{NO3}_i}$ does not differ significantly among the three subregions (Table 1 and Figure S3 in the supporting information). Note that these estimates do not account for dynamics in seasonal variability. For example, the dFe winter concentrations are conservative minimum values, because there may be continued flux of dFe from the seabed during the period of convective mixing.

In addition to the winter reserves, there are also sources of dFe and nitrate derived from MCDW, sea ice, and glacial ice. Each of these inputs was quantified using tracer experiments in the model hindcast (Figure 3). These sources are taken into account in calculating the apparent biological drawdown by adding the simulated dFe and nitrate concentrations from the closest model grid point *j* at the time of each observation *i*:

$$\widehat{\mathrm{dFe}_i} = \int_{\mathrm{EZ}}^{0} \mathrm{pos}\left(\widehat{\mathrm{dFe}_i} + \mathrm{dFe}_{\mathrm{MCDW}_j} + \mathrm{dFe}_{\mathrm{Sealce}_j} + \mathrm{dFe}_{\mathrm{Glaciallce}_j} - \mathrm{dFe}(z)_i\right)\mathrm{d}z$$

$$\widehat{\mathrm{NO3}_i} = \int_{\mathrm{EZ}}^{0} \mathrm{pos}\left(\widehat{\mathrm{NO3}_i} + \mathrm{NO3}_{\mathrm{MCDW}_j} + \mathrm{NO3}_{\mathrm{Sealce}_j} + \mathrm{NO3}_{\mathrm{Glaciallce}_j} - \mathrm{NO3}(z)_i\right)\mathrm{d}z$$

where *EZ* is the depth of the euphotic zone and pos indicates that only positive drawdowns are included in the integral. We do not have sufficient information to constrain spatial and temporal variations in the depth of the euphotic zone, so we utilized the mean mixed layer depth for the growing season (Table 1). This is justified on the basis that waters below the mixed layer account for only a small fraction of the vertically integrated primary production in this region [*Arrigo et al.*, 2008].

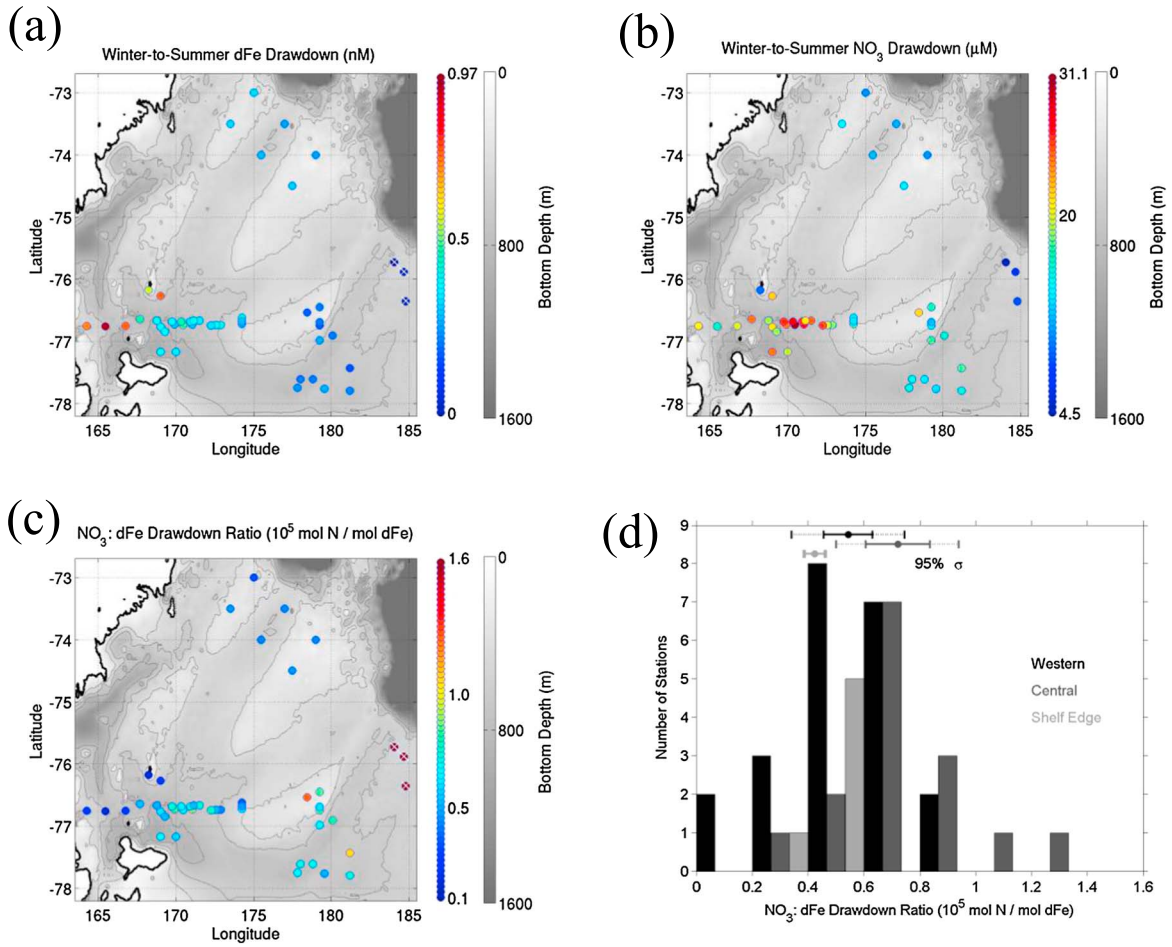

Figure 4. Dissolved (a) iron and (b) nitrate drawdown computed from the difference between cruise observations and the estimated winter reserve values plus cumulative inputs of dFe and nitrate from MCDW, sea ice, and glacial ice simulated for the space-time location of each station. Bathymetry shaded in gray with contours at 200 m intervals. (c, d) Nitrate:iron drawdown ratios. The histogram in Figure 4d displays regional estimates with bin sizes of $0.2 \cdot 10^5$ mol N (mol dFe)$^{-1}$. Note that the three easternmost shelf stations (white crosses in Figures 4a and 4c) are excluded in Figure 4d because summer surface dFe either exceeds or is nearly the same as the estimated winter reserve dFe, thereby making the drawdown ratios meaningless.

The drawdown ratio $\widetilde{NO3_i}/\widetilde{dFe_i}$ provides a means to evaluate phytoplankton uptake stoichiometry. Although there are hints of pan-regional patterns, systematic differences in the drawdown ratios are not statistically significant at the 95% confidence level (Figure 4), so we relied on the cruise-mean ratio (Table 1). Converting the NO_3:Fe drawdown ratio of $0.59 \pm 0.22 \times 10^5$ mol N (mol Fe)$^{-1}$ to carbon units yields a C:Fe molar ratio of 390,000 ± 150,000 (standard deviation) or equivalently 2.6 ± 0.99 μmol Fe:mol C. This value falls within the range of prior estimates for phytoplankton C:Fe assimilation ratios, which vary from 5000 to 450,000 [*Boyd et al.*, 2012; *Fung et al.*, 2000; *Twining et al.*, 2004], with some recent estimates as high as 2,500,000 [*Strzepek et al.*, 2011].

Using the phytoplankton C:Fe assimilation ratio inferred from our observations, we estimated seasonal biological iron demand with a satellite-based primary productivity algorithm applied to the Ross Sea shelf [*Arrigo et al.*, 2008] (Figure 1a). This bio-optical model of productivity is based on satellite retrievals of open water area and chlorophyll (Chl), together with estimates of irradiance and the phytoplankton C:Chl ratio. As such, it reflects net primary production, which consists of both new and recycled components. A synthesis of published values of the *f* ratio for the Ross Sea [*Asper and Smith*, 1999; *Cochlan and Bronk*, 2001; *Nelson and Smith*, 1986] (Table S1 in the supporting information) suggests $f = 0.5 \pm 0.1$. The demand for new carbon is scaled accordingly and converted to nitrogen units using the Redfield ratio. The corresponding iron demand is then computed using our empirical estimate of the drawdown ratio $\widetilde{NO3_i}/\widetilde{dFe_i}$ described above.

4. Discussion

Our observations and model results facilitate a quantitative comparison of annual dFe supply and demand in surface waters of the Ross Sea (Table 1). In aggregate, the mean supply and demand are approximately equal, and the difference between them is less than 10% of the estimated uncertainty. The two largest sources of dFe are the winter reserve (heavily influenced by benthic sources) and sea ice melt, providing roughly equal contributions that comprise more than 80% of the total. MCDW supplies most of the remainder, with the contribution from glacial ice almost an order of magnitude less.

Iron supply and demand estimates for the three subregions are also in approximate balance, with the magnitudes of the mean residuals ranging between 8% and 35% of the uncertainties. Curiously, regional differences in supply do not appear to be reflected in demand. Specifically, a higher winter reserve and larger input of sea ice melt in the western Ross Sea drive an iron supply approximately double that in the other subregions—whereas satellite-based estimates indicate highest iron demand in the central Ross Sea (although the uncertainties in the regional estimates overlap).

It is tempting to consider whether this lack of covariation in iron supply and demand could be a result of regional differences in phytoplankton composition that are not included in our estimates of demand. Blooms in the western Ross Sea tend to be dominated by diatoms, whereas those in the central subregion are more commonly dominated by the colonial prymnesiophyte *Phaeocystis antarctica* [*DiTullio and Smith*, 1996]. Cellular iron requirements of these two taxa certainly differ, but the literature does not offer consensus on a systematic relative difference in C:Fe ratios [*Strzepek et al*., 2011; *Tagliabue and Arrigo*, 2005]. Laboratory culture studies suggest lower Chl:C ratios in *P. antarctica* relative to a typical Antarctic diatom (*Fragilariopsis cylindrus*) [*Arrigo et al*., 2010], but these photophysiological differences run counter to the observed trend: all else being equal, if the bio-optical model were to include these variations in Chl:C, the relative difference in satellite-based productivity estimates in the west and central regions would be accentuated—with a commensurate impact on apparent iron demand. Thus, it does not appear that variations in phytoplankton composition can reconcile the regional trends in iron supply and demand. It is possible that these apparent discrepancies reflect undersampling of spatial and temporal variations in this complex and dynamic physical-biological-chemical environment, which is complicated by the fact that the western Ross Sea is ice covered longer than the other two subregions (Figure S7 in the supporting information). Alternatively, factors other than iron may be limiting or colimiting [*Boyd*, 2002]. However, the low concentrations of dFe observed in surface waters (Figure 1b) are consistent with iron limitation. In any case, the domain-wide average iron demand appears to be in balance with the supply processes quantified here, albeit with substantial uncertainty.

In light of these uncertainties, it is useful to quantify the error budget. On the demand side, the fractional error of 0.73 is dominated by uncertainty in the C:Fe ratio (0.37), which is approximately twice that ascribed to the *f* ratio (0.2). Uncertainty in the satellite retrieval of primary production itself is estimated to be 15% [*Arrigo et al*., 2008]. On the supply side, the fractional error is somewhat lower: 0.56. The two largest contributors are uncertainties in the winter reserve and sea ice sources. The former reflects purely observational uncertainty, as we have insufficient data to assess the accuracy of the wintertime mixed layer depths simulated by the model. The latter reflects uncertainty in the end-member concentration of dFe in sea ice (see section 2), as the modeled sea ice cover is consistent with observations (Figures S6, S7, and Table S2 in the supporting information). Absolute uncertainties in the contributions from MCDW and glacial ice are more than an order of magnitude lower and again reflect uncertainty in the end-member concentrations, as the hydrodynamic aspects of MCDW intrusions and glacial melt simulated by the model compare favorably with available observations (Figures S8 and S9 in the supporting information).

Additional uncertainties pertain to mechanisms of iron supply that we have not considered. Atmospheric deposition is thought to be very small in the Southern Ocean [*Mahowald et al*., 2005]. Analyses of snow from the Ross Sea [*Edwards and Sedwick*, 2001] suggest an aeolian flux of water-soluble iron on the order of 0.1 μmol Fe m^{-2} yr^{-1}, with locally higher deposition confined to the McMurdo Sound area [*Winton et al*., 2014]. Postconvective vertical mixing by turbulent diffusion and/or episodic upwelling by mesoscale and submesoscale fronts and eddies may supply additional dFe during the growing season. However, the vertical gradient on which these mechanisms operate is generally weak at the base of the euphotic zone (Figure S11 in the supporting information). The biological availability of suspended particulate iron [*Lam et al*., 2012], which we have not considered, is perhaps the most significant outstanding unknown in terms of dFe supply.

5. Conclusions

Despite the large uncertainties, this attempt to quantify proximate iron sources in the Ross Sea has revealed several important findings relative to estimated iron demand on an annual time scale. Direct measurement of the near-bottom dFe profile and its significance in terms of the vertically integrated inventory confirm the importance of benthic iron supply, which has been proposed in the Ross Sea [*Gerringa et al*., 2015; *Marsay et al*., 2014], elsewhere in the Southern Ocean [*Blain et al*., 2007; *de Jong et al*., 2012; *Tagliabue et al*., 2009; *Wadley et al*., 2014], as well as in other locations [*Johnson et al*., 1999]. In contrast to other areas on the Antarctic margin, where melting glacial ice is a major source of iron [*Gerringa et al*., 2012], the proportion of dFe supplied from glacial ice appears to be negligible in the Ross Sea: input from sea ice is an order of magnitude larger on a regional basis. Our findings illustrate the complexities of iron cycling in the Southern Ocean, highlighting the heterogeneity of the underlying processes along the Antarctic continental margin. Explicit representation of these complexities, and the temporal variability in both proximate and ultimate sources of iron, will be necessary to understand how a changing climate will affect this important ecosystem and its influence on biogeochemical cycles. Reduction of the present uncertainties in iron supply and demand will require coupled observational and modeling systems capable of resolving the wide range of physical, biological, and chemical processes involved.

Acknowledgments

The data used in this paper are archived at the Biological and Chemical Oceanography Data Management Office: http://www.bco-dmo.org/project/2155. Support of this research by the National Science Foundation's United States Antarctic Program is gratefully acknowledged. We thank the officers, crew, and technical personnel on board the R/V *Nathaniel B. Palmer* for their outstanding support during our seagoing operations. S. Howard and S. Springer assisted in adding tidal forcing to the circulation model. O. Kosnyrev, V. Kosnyrev, and L. Anderson provided technical support in data analysis and figure preparation. We thank two anonymous referees for their thorough reviews that helped improve the manuscript.

The Editor thanks two anonymous reviewers for their assistance in evaluating this paper.

References

Arrigo, K. R., D. L. Worthen, M. P. Lizotte, P. Dixon, and G. Dieckmann (1997), Primary production in Antarctic sea ice, *Science*, *276*(5311), 394–397.

Arrigo, K. R., G. R. DiTullio, R. B. Dunbar, D. H. Robinson, M. Van Woert, D. L. Worthen, and M. P. Lizotte (2000), Phytoplankton taxonomic variability in nutrient utilization and primary production in the Ross Sea, *J. Geophys. Res.*, *105*(C4), 8827–8846, doi:10.1029/1998JC000289.

Arrigo, K. R., D. L. Worthen, and D. H. Robinson (2003), A coupled ocean-ecosystem model of the Ross Sea. Part 2: Iron regulation of phytoplankton taxonomic variability and primary production, *J. Geophys. Res.*, *108*(C7), 3231, doi:10.1029/2001JC000856.

Arrigo, K. R., G. L. van Dijken, and S. Bushinsky (2008), Primary production in the Southern Ocean, 1997–2006, *J. Geophys. Res.*, *113*, C08004, doi:10.1029/2007JC004551.

Arrigo, K. R., M. M. Mills, L. R. Kropuenske, G. L. van Dijken, A.-C. Alderkamp, and D. H. Robinson (2010), Photophysiology in two major Southern Ocean phytoplankton taxa: photosynthesis and growth of *Phaeocystis antarctica* and *Fragilariopsis cylindrus* under different irradiance levels, *Integr. Comp. Biol.*, *50*(6), 950–966.

Asper, V. L., and W. O. Smith Jr. (1999), Particle fluxes during austral spring and summer in the southern Ross Sea, Antarctica, *J. Geophys. Res.*, *104*(C3), 5345–5359, doi:10.1029/1998JC900067.

Blain, S., et al. (2007), Effect of natural iron fertilization on carbon sequestration in the Southern Ocean, *Nature*, *446*(7139), 1070–1074.

Boyd, P. W. (2002), Environmental factors controlling phytoplankton processes in the Southern Ocean, *J. Phycol.*, *38*(5), 844–861.

Boyd, P. W., K. R. Arrigo, R. Strzepek, and G. L. van Dijken (2012), Mapping phytoplankton iron utilization: Insights into Southern Ocean supply mechanisms, *J. Geophys. Res.*, *117*, C06009, doi:10.1029/2011JC007726.

Carter, S. P., and H. A. Fricker (2012), The supply of subglacial meltwater to the grounding line of the Siple Coast, West Antarctica, *Ann. Glaciol.*, *53*(60), 267–280.

Coale, K. H., R. M. Gordon, and X. Wang (2005), The distribution and behavior of dissolved and particulate iron and zinc in the Ross Sea and Antarctic circumpolar current along 170°W, *Deep Sea Res., Part I*, *52*, 295–318.

Cochlan, W. P., and D. A. Bronk (2001), Nitrogen uptake kinetics in the Ross Sea, Antarctica, *Deep Sea Res., Part II*, *48*(19–20), 4127–4153.

de Jong, J., V. Schoemann, D. Lannuzel, P. Croot, H. de Baar, and J.-L. Tison (2012), Natural iron fertilization of the Atlantic sector of the Southern Ocean by continental shelf sources of the Antarctic Peninsula, *J. Geophys. Res.*, *117*, G01029, doi:10.1029/2011JG001679.

de Jong, J., V. Schoemann, N. Maricq, N. Mattielli, P. Langhorne, T. Haskell, and J.-L. Tison (2013), Iron in land-fast sea ice of McMurdo Sound derived from sediment resuspension and wind-blown dust attributes to primary productivity in the Ross Sea, Antarctica, *Mar. Chem.*, *157*, 24–40.

Death, R., J. L. Wadham, F. Monteiro, A. M. L. Brocq, M. Tranter, A. Ridgwell, S. Dutkiewicz, and R. Raiswell (2014), Antarctic ice sheet fertilises the Southern Ocean, *Biogeosciences*, *11*, 2635–2643.

Dinniman, M. S., J. M. Klinck, and W. O. Smith Jr. (2011), A model study of Circumpolar Deep Water on the West Antarctic Peninsula and Ross Sea continental shelves, *Deep Sea Res., Part II*, *58*(13–16), 1508–1523.

DiTullio, G. R., and W. O. Smith Jr. (1996), Spatial patterns in phytoplankton biomass and pigment distributions in the Ross Sea, *J. Geophys. Res.*, *101*(C8), 18,467–18,477, doi:10.1029/96JC00034.

Edwards, R., and P. Sedwick (2001), Iron in East Antarctic snow: Implications for atmospheric iron deposition and algal production in Antarctic waters, *Geophys. Res. Lett.*, *28*(20), 3907–3910, doi:10.1029/2001GL012867.

Fitzwater, S. E., K. S. Johnson, R. M. Gordon, K. H. Coale, and W. O. Smith Jr. (2000), Trace metal concentrations in the Ross Sea and their relationship with nutrients and phytoplankton growth, *Deep Sea Res., Part II*, *47*, 3159–3179.

Fung, I. Y., S. K. Meyn, I. Tegen, S. C. Doney, J. G. John, and J. K. B. Bishop (2000), Iron supply and demand in the upper ocean, *Global Biogeochem. Cycles*, *14*(1), 281–295, doi:10.1029/1999GB900059.

Gerringa, L. J. A., A.-C. Alderkamp, P. Laan, C.-E. Thuróczy, H. J. W. De Baar, M. M. Mills, G. L. van Dijken, H. V. Haren, and K. R. Arrigo (2012), Iron from melting glaciers fuels the phytoplankton blooms in Amundsen Sea (Southern Ocean): Iron biogeochemistry, *Deep Sea Res., Part II*, *71–76*, 16–31.

Gerringa, L. J. A., P. Laan, G. L. van Dijken, H. van Haren, H. J. W. De Baar, K. R. Arrigo, and A. C. Alderkamp (2015), Sources of iron in the Ross Sea polynya in early summer, *Mar. Chem.*, doi:10.1016/j.marchem.2015.06.002, in press.

Gordon, L. I., L. A. Codispoti, J. C. Jennings Jr., F. J. Millero, J. M. Morrison, and C. Sweeney (2000), Seasonal evolution of hydrographic properties in the Ross Sea, Antarctica, 1996–1997, *Deep Sea Res., Part II*, *47*(15–16), 3095–3117.

Jacobs, S. S., and C. F. Giulivi (1999), Thermohaline data and ocean circulation on the Ross Sea continental shelf, in *Oceanography of the Ross Sea Antarctica*, edited by G. Spezie and G. M. R. Manzella, pp. 3–16, Springer, Milan.

Johnson, K. S., F. P. Chavez, and G. E. Friederich (1999), Continental-shelf sediment as a primary source of iron for coastal phytoplankton, *Nature*, *398*(6729), 697–700.

Lam, P. J., D. C. Ohnemus, and M. A. Marcus (2012), The speciation of marine particulate iron adjacent to active and passive continental margins, *Geochim. Cosmochim. Acta*, *80*, 108–124.

Lannuzel, D., V. Schoemann, J. de Jong, B. Pasquer, P. van der Merwe, F. Masson, J.-L. Tison, and A. Bowie (2010), Distribution of dissolved iron in Antarctic sea ice: Spatial, seasonal, and inter-annual variability, *J. Geophys. Res.*, *115*, G03022, doi:10.1029/2009JG001031.

Mahowald, N. M., A. R. Baker, G. Bergametti, N. Brooks, R. A. Duce, T. D. Jickells, N. Kubilay, J. M. Prospero, and I. Tegen (2005), Atmospheric global dust cycle and iron inputs to the ocean, *Global Biogeochem. Cycles*, *19*, GB4025, doi:10.1029/2004GB002402.

Marsay, C. M., P. N. Sedwick, M. S. Dinniman, P. M. Barrett, S. L. Mack, and D. J. McGillicuddy (2014), Estimating the benthic efflux of dissolved iron on the Ross Sea continental shelf, *Geophys. Res. Lett.*, *41*, 7576–7583, doi:10.1002/2014GL061684.

Martin, J. H., R. M. Gordon, and S. E. Fitzwater (1990), Iron in Antarctic waters, *Nature*, *345*, 156–158.

Measures, C. I., M. Hatta, and M. M. Grand (2012), Bioactive trace metal distributions and biogeochemical controls in the Southern Ocean, *Oceanography*, *25*(3), 122–133.

Nelson, D. M., and W. O. Smith Jr. (1986), Phytoplankton bloom dynamics of the western Ross Sea ice edge—II. Mesoscale cycling of nitrogen and silicon, *Deep Sea Res.*, *33*(10), 1389–1412.

Orsi, A. H., and C. L. Wiederwohl (2009), A recount of Ross Sea waters, *Deep Sea Res., Part II*, *56*, 778–795.

Raiswell, R., M. Tranter, L. G. Benning, M. Siegert, R. De'ath, P. Huybrechts, and T. Payne (2006), Contributions from glacially derived sediment to the global iron (oxyhydr)oxide cycle: Implications for iron delivery to the oceans, *Geochim. Cosmochim. Acta*, *70*(11), 2765–2780.

Sedwick, P. N., G. R. DiTullio, and D. J. Mackey (2000), Iron and manganese in the Ross Sea, Antarctica: Seasonal iron limitation in Antarctic shelf waters, *J. Geophys. Res.*, *105*(C5), 11,321–11,336, doi:10.1029/2000JC000256.

Sedwick, P. N., et al. (2011), Early season depletion of dissolved iron in the Ross Sea polynya: Implications for iron dynamics on the Antarctic continental shelf, *J. Geophys. Res.*, *116*, C12019, doi:10.1029/2010JC006553.

Spolaor, A., P. Vallelonga, G. Cozzi, J. Gabrieli, C. Varin, N. Kehrwald, P. Zennaro, C. Boutron, and C. Barbante (2013), Iron speciation in aerosol dust influences iron bioavailability over glacial-interglacial timescales, *Geophys. Res. Lett.*, *40*, 1618–1623, doi:10.1002/grl.50296.

Strzepek, R. F., M. T. Maldonado, K. A. Hunter, R. D. Frew, and P. W. Boyd (2011), Adaptive strategies by Southern Ocean phytoplankton to lessen iron limitation: Uptake of organically complexed iron and reduced cellular iron requirements, *Limnol. Oceanogr.*, *56*, 1983–2002.

Sunda, W. G., and S. A. Huntsman (1997), Interrelated influence of iron, light and cell size on marine phytoplankton growth, *Nature*, *390*(6658), 389–392.

Tagliabue, A., and K. R. Arrigo (2005), Iron in the Ross Sea: 1. Impact on CO_2 fluxes via variation in phytoplankton functional group and non-Redfield stoichiometry, *J. Geophys. Res.*, *110*, C03009, doi:10.1029/02004JC002531.

Tagliabue, A., L. Bopp, and O. Aumont (2009), Evaluating the importance of atmospheric and sedimentary iron sources to Southern Ocean biogeochemistry, *Geophys. Res. Lett.*, *36*, L13601, doi:10.1029/2009GL038914.

Twining, B. S., S. B. Baines, N. S. Fisher, and M. R. Landry (2004), Cellular iron contents of plankton during the Southern Ocean Iron Experiment (SOFeX), *Deep Sea Res., Part I*, *51*(12), 1827–1850.

Wadley, M. R., T. D. Jickells, and K. J. Heywood (2014), The role of iron sources and transport for Southern Ocean productivity, *Deep Sea Res., Part I*, *87*, 82–94.

Winton, V. H. L., G. B. Dunbar, N. A. N. Bertler, M. A. Millet, B. Delmonte, C. B. Atkins, J. M. Chewings, and P. Andersson (2014), The contribution of aeolian sand and dust to iron fertilization of phytoplankton blooms in southwestern Ross Sea, Antarctica, *Global Biogeochem. Cycles*, *28*, 423–436, doi:10.1002/2013GB004574.

Auxiliary Material for

Iron supply and demand in an Antarctic shelf ecosystem

D.J. McGillicuddy, Jr.[1*], P.N. Sedwick[2], M.S. Dinniman[2], K.R. Arrigo[3], T.S. Bibby[4], B.J.W. Greenan[5], E.E. Hofmann[2], J.M. Klinck[2], W.O. Smith, Jr.[6], S.L. Mack[2], C.M. Marsay[2†], B.M. Sohst[2], and G.L. van Dijken[3]

[1]Woods Hole Oceanographic Institution, Woods Hole, Massachusetts 02543, USA,

[2]Department of Ocean, Earth and Atmospheric Sciences, Old Dominion University, Norfolk, Virginia 23529, USA,

[3]Department of Environmental Earth System Science, Stanford University, Stanford, California 94305, USA,

[4]Ocean and Earth Science, National Oceanography Centre Southampton, University of Southampton, Southampton SO14 3ZH, UK,

[5]Ocean and Ecosystem Sciences Division, Bedford Institute of Oceanography, Department of Fisheries and Oceans, Dartmouth B2Y 4A2, Canada,

[6]Virginia Institute of Marine Science, College of William and Mary, Gloucester Point, Virginia 23062, USA,

[†]Now at Skidaway Institute of Oceanography, University of Georgia, 10 Science Circle, Savannah, Georgia 31411, USA

*email: dmcgillicuddy@whoi.edu

Geophysical Research Letters, June 2015

Introduction

This document provides supplementary information describing the methods used in this study as well as additional figures and tables substantiating statements made in the main article.

Contents

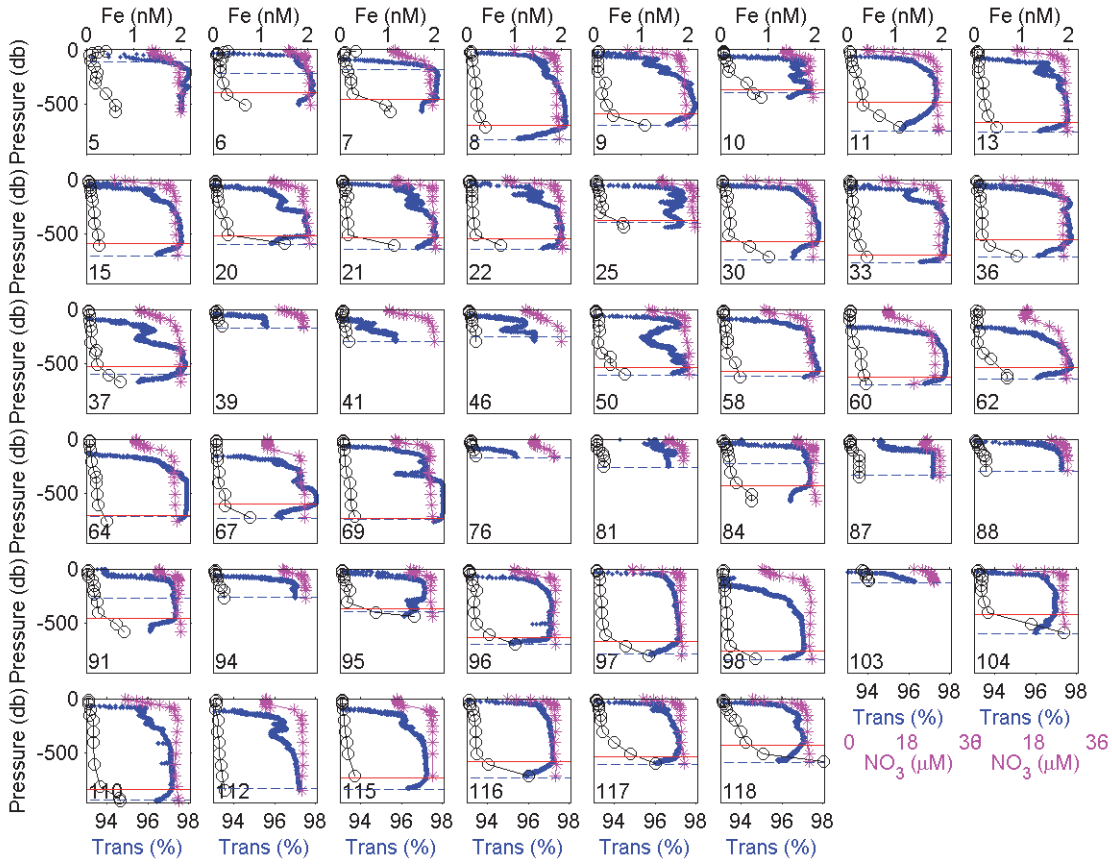

Figure S1. Dissolved iron concentration (open circles), nitrate (magenta plus signs) and CTD transmissometer profiles (solid blue lines). Red lines indicate the upper bounds of benthic nepheloid layers, subjectively identified as profiles in which beam transmission (measured with a WET Labs C-Star with factory calibrations) decreases with depth near the bottom. Blue dashed lines show the maximum mixed layer depth for each location diagnosed from the ROMS hindcast for the PRISM era. Numerals in the lower left of each panel indicate the cast number (not station number).

Definition of the regional subdomains. Choice of the regional subdomains for this analysis was informed by their biological and biogeochemical characteristics. For example, the western subdomain roughly coincides with the largest dFe input due to melting sea ice (Figure 3a). Glacial ice melt input penetrates farthest into the interior of the central subdomain (Figure 3b), although that input is relatively modest. The shelf edge subdomain generally corresponds to the area of lower primary productivity offshore (Figure 1a).

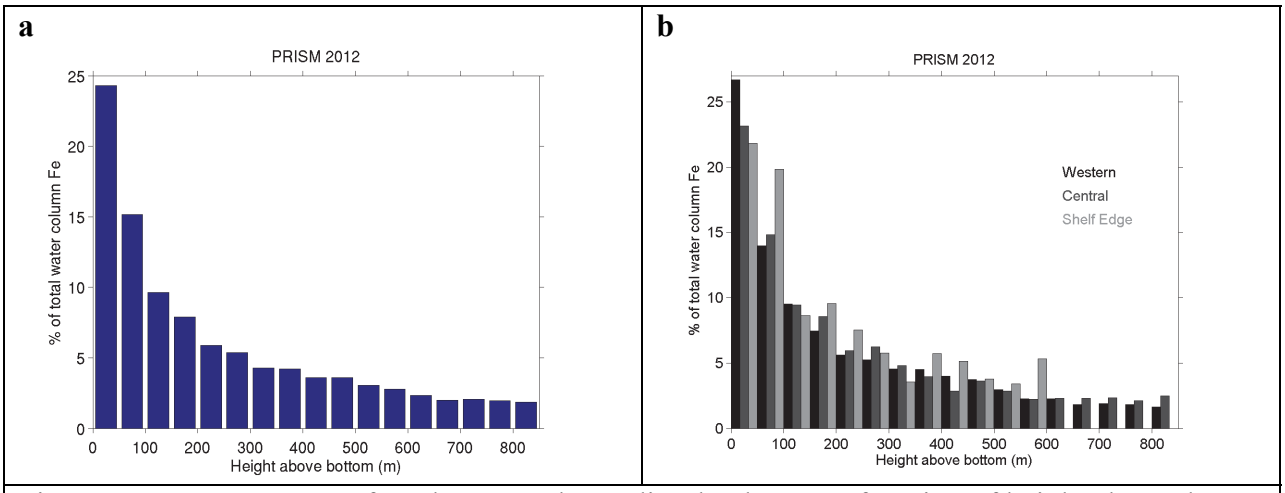

Figure S2. **a**, Percentage of total water column dissolved Fe as a function of height above the bottom. **b**, Same as **a**, but broken down into the three regional subdomains indicated in Figure 1**a**. Only casts in water depths greater than 300 m are included in panels **a** and **b**.

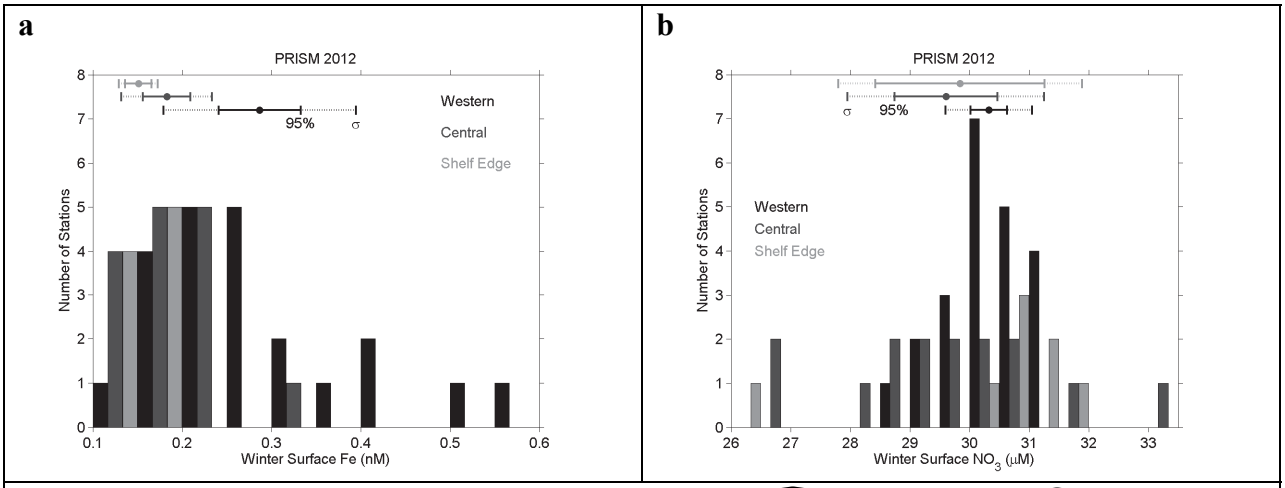

Figure S3. Estimated wintertime surface mixed layer iron $\widehat{dFe_t}$ (**a**) and nitrate $\widehat{NO3_t}$ (**b**) concentrations, displayed as histograms for the three subregions indicated in Figure 1a.

Satellite-based estimates of net primary productivity (NPP). Because our estimates of iron supply involve multi-year processes such as transport of MCDW and glacial melt from within the Ross Ice Shelf (RIS) cavity, we compute a long-term mean (1997-2013) of NPP. For the years 1997 through 2002, surface Chl *a* concentrations were determined from Level 3 (8-day binned, 9 km resolution) of the most recently reprocessed SeaWiFS ocean color data (Reprocessing R2010.0) using the OC4v6 algorithm (http://oceancolor.gsfc.nasa.gov/REPROCESSING/R2009/ocv6/), a modified version of the OC4v4 algorithm. For the years 2002 through 2013, surface Chl *a* concentrations were determined from Level 3 MODIS Aqua ocean color data (Reprocessing R2010.0 for the years 2002-2010 and R2013.0 for 2011 onwards) using the OC3Mv6 algorithm. Daily sea surface temperature (SST) is based on the Reynolds Optimally Interpolated SST (OISST) Version 2

product obtained from NOAA (http://www.emc.ncep.noaa.gov/research/cmb/sst_analysis/). Sea ice cover was estimated from Special Sensor Microwave Imager (SSM/I) 37 and 85 GHz bands using the Polynya Signature Simulation Method (PSSM) algorithm, which allows determination of sea ice presence/absence at 6.25 km resolution. According to this algorithm, a given pixel is defined as being ice covered wherever the sea ice concentration is greater than approximately 10%. Calculating open water areas using different thresholds (10%, 50%, 90%) yields similar results. This results from the fact that only a very small fraction of the Ross Sea has ice concentrations between 10% and full ice cover, and the gradient in sea ice concentration between open water and 100% (or close to that) is very sharp.

Time-series of NPP reveal substantial interannual variability, both within the three subregions as well as the domain-wide averages (Figure S4). This interannual variability is factored into the uncertainty estimates of iron demand reported in Table 1. We note that the 2011-2012 values for NPP are not very different from their long-term means, suggesting that the PRISM measurements come from a time period that is representative of "average" conditions.

Nelson and Smith, 1986		
	Date	f-ratio
	Jan 1983	0.53
	Jan 1983	0.37
	Jan 1983	0.44
	Jan 1983	0.54
	Jan 1983	0.46
	Jan 1983	0.33
	Jan 1983	0.35
	Jan 1983	0.48
	Jan 1983	0.63
	Jan 1983	0.39
	Jan 1983	0.37
	Jan 1983	0.28
	Jan 1983	0.22
	Feb 1983	0.29
	Feb 1983	0.24
Asper and Smith, 1999		
	Dec 1995	0.89
	Dec 1995	0.64
Cochlan and Bronk, 2001		
	Dec 1997	0.93
	Dec 1997	0.83
	Jan 1997	0.91
	Jan 1997	0.44
	Feb 1997	0.31
	Feb 1997	0.54
Month	Average	Standard deviation
Dec	0.82	0.13
Jan	0.45	0.16
Feb	0.34	0.13
Dec-Feb	0.54	0.14

Table S1. Compilation of estimates of the f-ratio in the Ross Sea. Values from Nelson and Smith (1986) computed from the nitrate and ammonium uptake rates in their Table 1. Values from Asper and Smith (1999) extracted directly from their Table 3. For Cochlan and Bronk (2001), nitrate and ammonium uptake rates were computed using observed nutrient concentrations (their Table 1) and fitted Michaelis-Menten parameters (their Table 2).

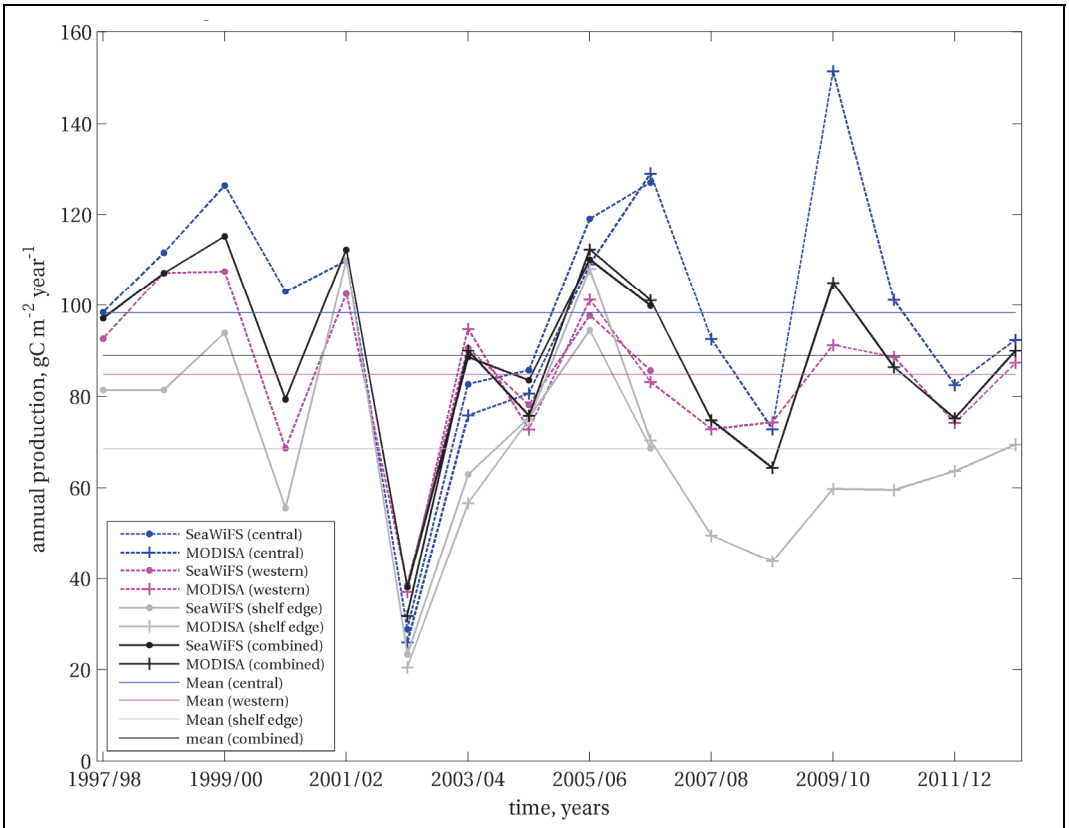

Figure S4. Time-series of satellite-based estimates of NPP (SeaWiFS and MODIS-A) for the central, western, and shelf-edge subdomains as well as domain-wide averages.

Estimation of the f-ratio. Published values for the period December-February were compiled from three sources [*Asper and Smith*, 1999; *Cochlan and Bronk*, 2001; *Nelson and Smith*, 1986] (Table S1). These measurements span multiple years and locations within the Ross Sea. Overall there is a tendency for the f-ratio to be higher early in the growing season and lower later on. Monthly averages and standard deviations were calculated from the compilation, and these were subsequently averaged to obtain seasonal estimates and associated uncertainties.

Tracer transport modeling. The hydrodynamic model is based upon earlier simulations of the Ross Sea [*Dinniman et al.*, 2011] with the addition of tidal forcing [*Padman et al.*, 2002] as well as a dynamic sea ice component [*Budgell*, 2005]. After a six year spin-up, a tracer with an initial concentration of 100.0 representing CDW is placed in water seaward of the continental shelf (defined by the 1200 m isobath) at all depths where the temperature is greater than 0.0°C. The sea ice and glacial ice tracers are initialized to zero everywhere in the model domain. All three tracers are advected and diffused over the entire model domain (Figure S5). There is no surface or bottom flux of the CDW tracer, but there is a continuous source at inflow boundaries that meet the CDW criteria. The sea ice tracer enters the model domain as a surface flux computed from melting of both the top and bottom sea ice surfaces. The glacial melt tracer enters as a surface flux computed from melting at the base of any floating ice shelves. Neither of the two ice melt tracers receive any contribution from the open boundaries, and the tracers are free to advect out of the model domain.

Uptake of dFe by phytoplankton is not explicitly represented, so cumulative iron supply is estimated from the dFe inventory in the euphotic zone at the end of the growing season. Given the capacity for rapid utilization of dFe delivered to the upper layers, this approach may allow for unrealistic lateral transport within the euphotic zone during the growing season. However, the gradients in tracer distributions are such that horizontal fluxes of euphotic-zone dFe between our chosen subdomains are likely to be relatively small, with the possible exception of that derived from MCDW (Figure 3). We note that MCDW is a year-round source of dFe, and the unrealistic transport within the euphotic zone would be confined to the ice-free growing season, which is roughly one-quarter to one-third of the year. As such, we expect minimal impact on regional partitioning of the dFe supply reported in Table 1.

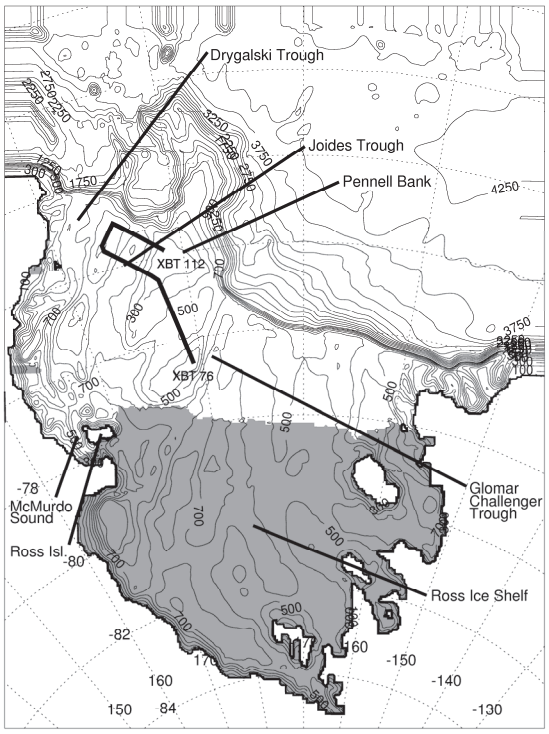

Figure S5. Model domain. Ross Ice Shelf shaded in gray. XBT section from Figure S8 shown in bold, with XBT station numbers indicated at the endpoints.

Scavenging of iron onto sinking particles results in loss of dissolved iron along the transport pathways. A variety of approaches have been used to simulate this process, including sophisticated biogeochemical models [*Archer and Johnson*, 2000; *Moore and Braucher*, 2008; *Parekh et al.*, 2004]. In the absence of a detailed region-specific iron cycling model for the Ross Sea, we used the simple scavenging model of Johnson et al. [1997]. Specifically, the Johnson et al. model represents scavenging loss R as a first-order reaction operating on the difference between dFe and the effective solubility dFe_{soly}: $R = k_{Fe}\left(dFe - dFe_{soly}\right)$. Johnson et al. use dFe_{soly} = 0.6 nM, and k_{Fe} = 0.005 yr^{-1}. In the upper ocean, rapid uptake of iron by phytoplankton decreases dFe concentrations to levels below that which can support precipitation into the particulate phase [*Boyd and Ellwood*, 2010], so we neglect this process in surface waters. Indeed, our data are consistent with rapid drawdown of dFe to ~0.1 nM during the austral spring bloom [*Sedwick et al.*, 2011], well below the concentration at which the Johnson et al. [1997] model would predict scavenging. As such, our dFe supply estimates for the winter reserve and sea ice sources are unaffected. However, MCDW and a portion of the glacial ice source transit at mid depths before they are ventilated and dFe is delivered to the surface layer. The measured end-member dFe concentration used for MCDW is 0.27 ± 0.05 nM (Figure 1b), which is again less than the effective solubility value dFe_{soly}—hence the Johnson et al. [1997] model predicts no scavenging for this source. The end-member dFe concentration for glacial ice meltwater is 29 ± 21 nM, so scavenging is computed explicitly in those tracer transport simulations. Iron removal by scavenging has only a minor impact on the results, not enough to affect the two significant figures reported in Table 1 for the glacial ice source. We assessed the sensitivity of this result by repeating the simulation with a "high" scavenging parameter set (dFe_{soly} = 0.4 nM, and k_{Fe} = 0.03 yr^{-1}), and again the difference

in the glacial ice source was not large enough to be captured by the two significant figures provided in Table 1.

Evaluation of the sea ice component of the model. Sea ice area for each grid cell is computed by the product of the sea ice concentration and the grid cell area. On a domain-wide basis, the model has too much ice at the maximum extent compared with observations, and is too slow to remove the ice during November (Figure S6, left column). The difference at maximum extent is primarily associated with the modeled characteristics of pack ice rather than the total area covered by high ice concentrations: specifically, the simulated pack ice has higher concentrations than indicated by the satellite observations. The model does well in bringing the ice back in fall and simulating the timing and ice area at the summer minimum. The comparison over just the continental shelf (Figure S6, right column) is qualitatively similar to that over the entire model domain, although the interannual difference in the minimum ice extent is simulated more accurately. Correlation coefficients and Willmott skill scores [*Willmott*, 1981] provide quantitative metrics of the congruence between simulated and observed sea ice area (Table S2).

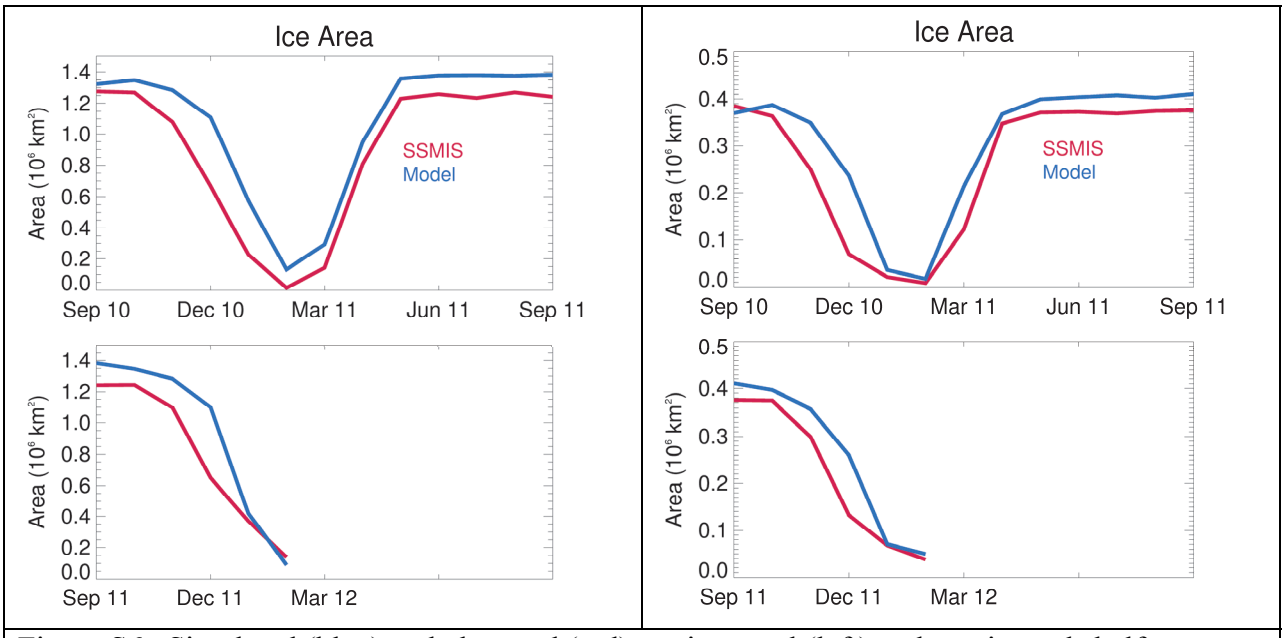

Figure S6. Simulated (blue) and observed (red) sea ice: total (left) and continental shelf (right). Adapted from Stern et al. [2013]. Observations are extracted from: Cavalieri, D. J., C. L. Parkinson, P. Gloersen, and H. Zwally. 1996, updated yearly. Sea Ice Concentrations from Nimbus-7 SMMR and DMSP SSM/I-SSMIS Passive Microwave Data. Boulder, Colorado USA: NASA DAAC at the National Snow and Ice Data Center.

	Correlation coefficient	Willmott skill score
Domain-wide	0.962	0.952
Continental shelf	0.949	0.951

Table S2. Skill evaluation of the simulated sea ice area.

Comparison of the distribution of modeled sea ice concentrations to satellite data show that the simulated polynya is similar in size and shape to the observations in late December (Figure S7, left column). The modeled ice edge is sharper than the observations, but that may be due in part to the resolution of the SSMIS data product (25 km) and its interpolation onto the 5 km resolution grid of the model. The observations document expansion of the polynya through January, with a thin strip of sea ice present near the shelf edge (Figure S7, middle and right columns). That aspect is not captured by the model, insofar as the entire offshore area is ice covered in late December, becoming ice free by the end of January.

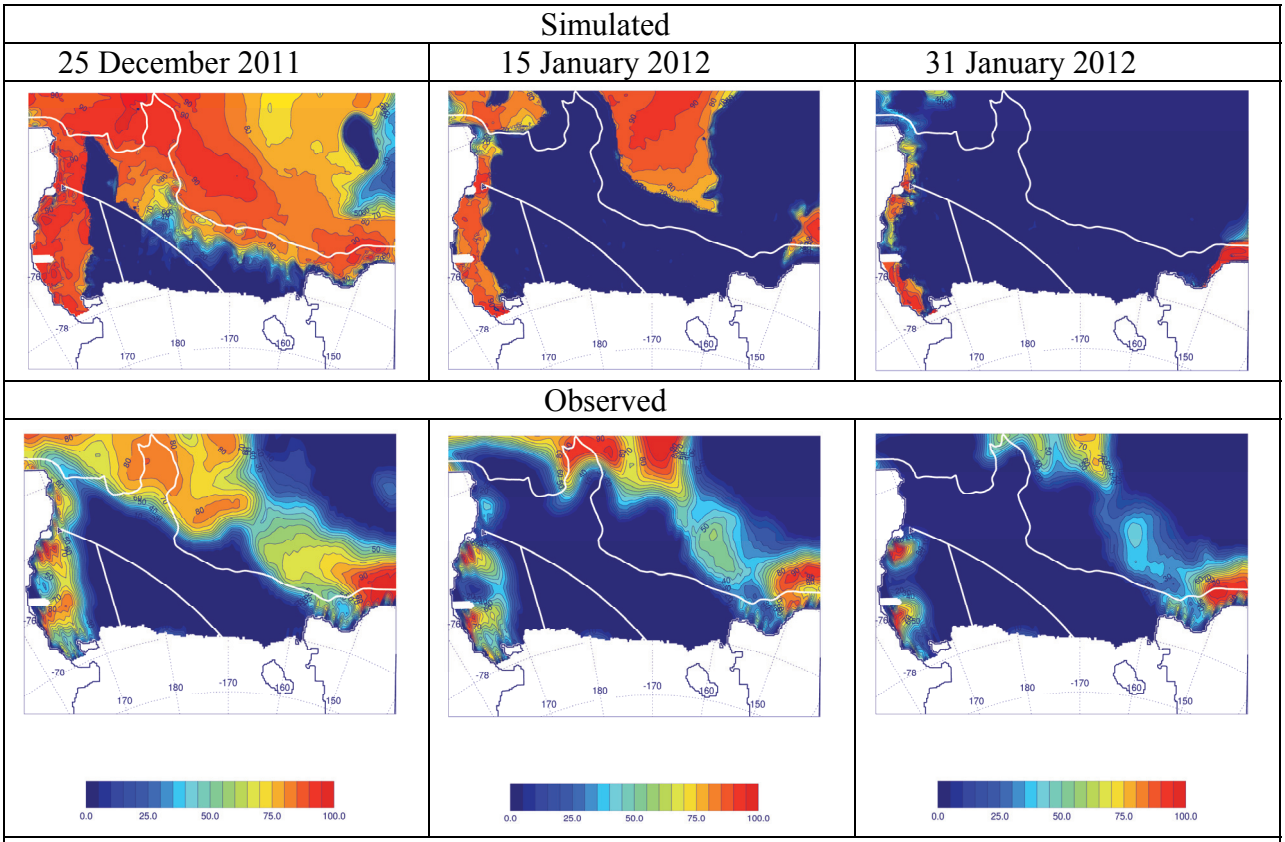

Figure S7. Simulated (top) and observed (bottom) sea ice concentrations (percent): 25 December 2011 (left), 15 January 2012 (middle), and 31 January 2012 (right). Observations are extracted from: Cavalieri, D. J., C. L. Parkinson, P. Gloersen, and H. Zwally. 1996, updated yearly. Sea Ice Concentrations from Nimbus-7 SMMR and DMSP SSM/I-SSMIS Passive Microwave Data. Boulder, Colorado USA: NASA DAAC at the National Snow and Ice Data Center. White lines show the boundaries between the three regional subdomains depicted in Figure 1: western, central, and shelf edge. Note the offshore limit of the shelf edge domain is defined by the 1200 m isobath because the source of CDW in the tracer simulation was assumed to be seaward of that boundary.

Evaluation of simulated CDW intrusions. It has been previously shown [*Dinniman et al.*, 2011] that the model generally reproduces the observed pathways of CDW intrusions onto and across the continental shelf and into the cavity beneath the RIS. A comparison of the simulated

and observed temperature structure in cross-sections across Ross, Pennell, and Mawson Banks and Joides Trough (Figure S8) facilitates phenomenological evaluation of the modeled intrusions. Clearly, there are systematic differences between the model and observations. First, the modeled mixed layer depth is too shallow and laterally homogeneous relative to the XBT measurements. The latter aspect may reflect aliasing of temporal variability into spatial variability due to the time period required to acquire the observations, whereas the model results are reported as a one-day average at the midpoint in time. Another systematic difference is that the simulated MCDW intrusions (identified by mid-depth areas of relatively warm temperatures either above or just to west of the banks) are warmer than observed, except on top of Mawson Bank (stations 98-103) where the intrusion may be too weak. However, the locations and vertical extent of the simulated MCDW intrusions, especially on top of and west of Pennell Bank, are generally consistent with observations.

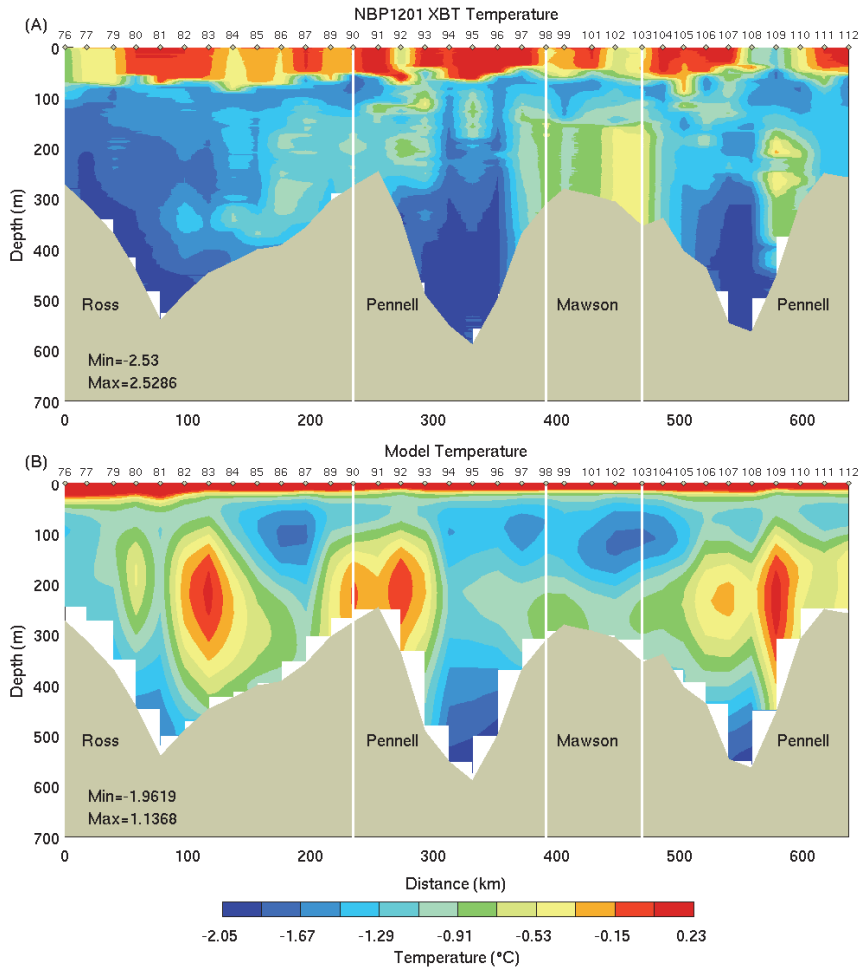

Figure S8. Observed (top) and simulated (bottom) temperature distributions along the XBT transects indicated in Figure S5. Observations were collected 27-28 January 2012, whereas the model results are reported as a one-day average at the midpoint in time. Vertical white lines indicate the turning points of the sections.

There are few observational estimates of the volume transport onto the Ross Sea continental shelf with which the model can be evaluated. Recently, Kohut et al. [2013] estimated MCDW transport using velocity from a mooring deployed on the western slope of Pennell Bank (Figure S5) from 27 January to 9 February 2011 together with several hydrographic sections to delineate the extent of MCDW. Their results indicate the mean transport of MCDW along the west side of the bank to be 0.24 Sv towards the south. Model estimates of the flow through the same cross section (Figure S9) give a somewhat lower annual mean transport (0.14 ± 0.07 Sv) southward along the slope, but there is stronger transport in summer (0.17 ± 0.06 Sv) that is

closer to the observations. The model transport over the actual period of the mooring deployment (0.22 ± 0.03 Sv) is quite close to the Kohut et al. estimate.

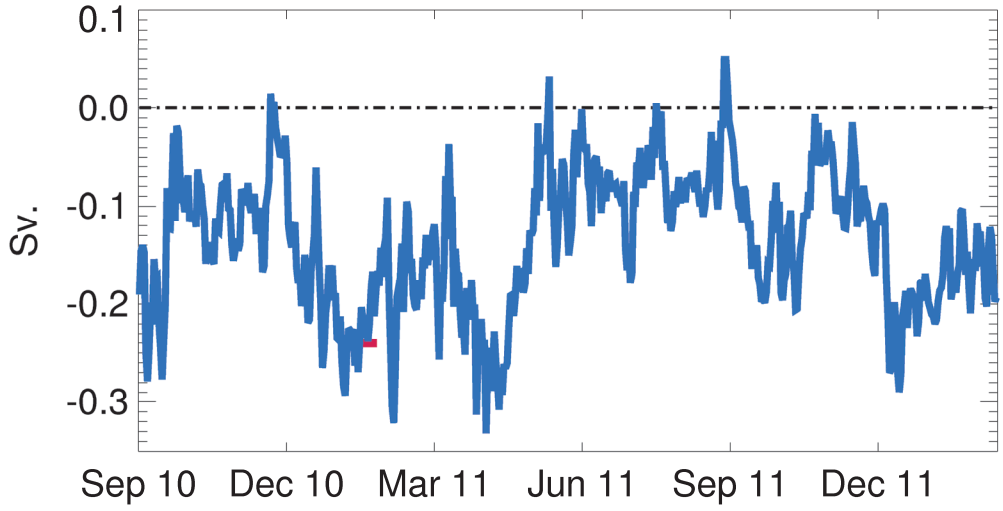

Figure S9. Simulated (blue) and observed [*Kohut et al.*, 2013] (red) MCDW transport.

Evaluation of the simulated glacial melt and associated dFe concentrations. The model melt rate over the last year of the simulation averaged over the entire base of the Ross Ice Shelf is 22 ± 7 cm yr^{-1}, larger than the 15 cm yr^{-1} average in the earlier model [*Dinniman et al.*, 2011], but still within the range of observations (8-22 cm yr^{-1}) [*Jacobs et al.*, 1992; *Lingle et al.*, 1991; *Loose et al.*, 2009; *Shabtaie and Bentley*, 1987]. The present simulation pertains to a different time period than the prior model [*Dinniman et al.*, 2011], and interannual variations in the ice shelf basal melt rate have been observed [*Loose et al.*, 2009]. In the model, interannual changes in the ice shelf basal melt are mostly due to interannual changes in the summer polynya extent. However, we suspect that at least some of the difference from the previous model is due to changes in the vertical mixing over the continental shelf because of the addition of the dynamic sea ice model. The previous model imposed the sea ice concentrations from satellite observations and thus likely better represented the winter coastal polynyas. This would lead to more vertical mixing on the shelf compared to the current model, resulting in lower temperatures of the MCDW on the shelf and lower melt rates. We note that the model does not simulate the input of fresh water from the grounded portion of the ice sheet into the RIS cavity. However, that flux is thought to contribute a small fraction (~5%) of the freshwater budget for the RIS [*Carter and Fricker*, 2012]. Moreover, the Ross Sea receives a relatively small amount of basal meltwater compared with other regions around Antarctica [*Rignot et al.*, 2013].

Simulated dFe concentrations in the Ice Shelf Water (ISW) emanating from underneath the RIS generally range between 5-15 pM at a depth of 450m (Figure S10a), with a maximum of ca. 30 pM at shallower depths. These concentrations are approximately an order of magnitude less than dFe observed in the supercooled waters (T < -1.8ºC, depth 300-600m) in a section occupied along the RIS (Figure S10b,c), consistent with modest supply of dFe from glacial ice melt. Note that if our assumed end-member concentration of $dFe_{GlacialIce}$ = 29 ± 21 nM (see

Methods section 2.2) were increased by 2-3 orders of magnitude as suggested by Death et al. [2014], the simulated dFe concentrations from glacial meltwater would exceed the observed total dFe concentrations in that water mass (Figure S10c) by a wide margin. As such, our choice of the lower end-member based on the Talos Dome ice cores seems more appropriate for this region.

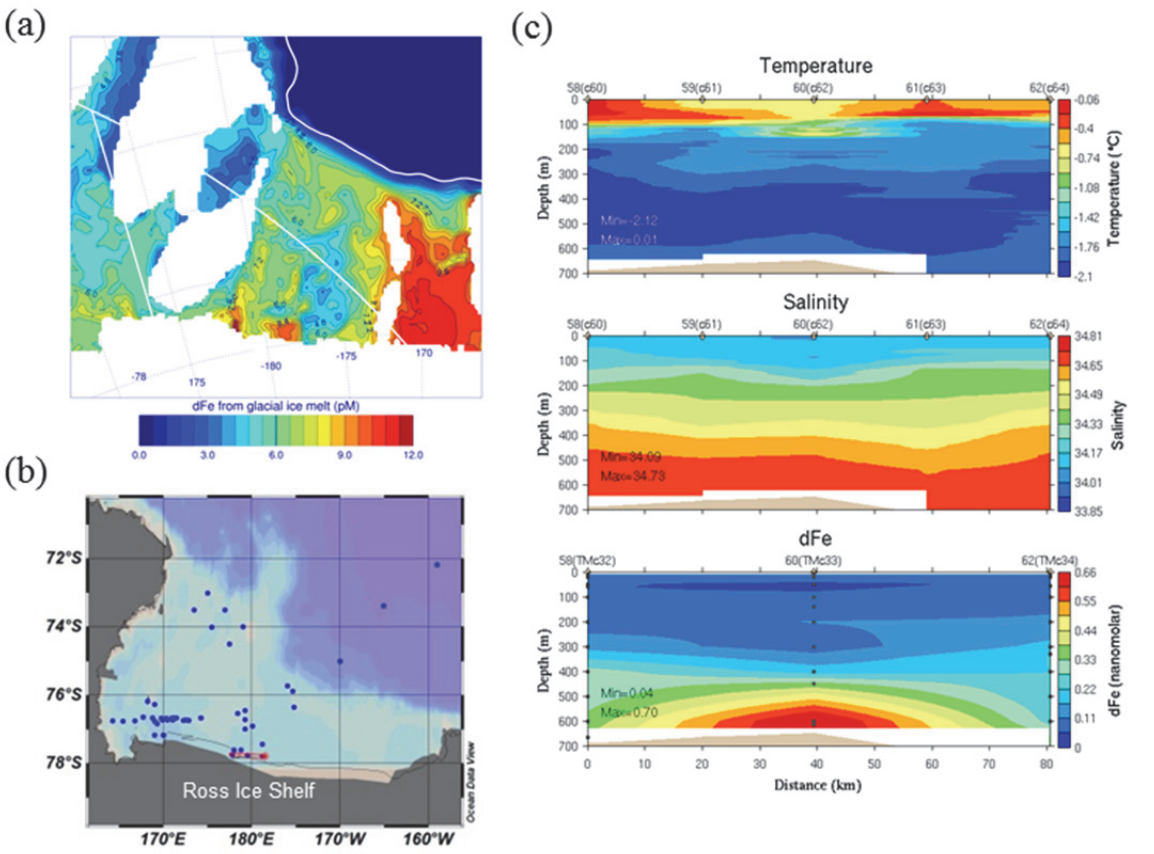

Figure S10. (a) Simulated dFe concentration at 450m derived from glacial meltwater from an example 1-day average taken from 25 January 2012. (b) Locations of dFe measurements (cf. Figure 1a), with a red rectangle around the stations included in the transect presented in panel (c). Temperature and salinity in panel (c) come from high-resolution CTD data, whereas dots in the lower panel indicate the discrete measurements of dFe in the water column.

Comparison of simulated sea ice and glacial melt dFe supplies with estimates based on meltwater inventories. An upper bound on the volume of sea ice meltwater can be derived by assuming all sea ice melts in place. This is clearly an overestimate because the Ross Sea is a net exporter of ice [*Comiso et al.*, 2011; *Kwok*, 2005]. Taking the wintertime ice thickness over the continental shelf to be 0.3-0.9 m [*Jeffries and Adolphs*, 1997], the dFe concentration in sea ice to be 10 nM (see **Methods**), and a summertime mixed layer of 10-30 m [*Fragoso and Smith*, 2012], the annual supply of dFe from sea ice would be 100-900 pM. As expected, the model-based estimate of 126 pM falls on the lower end of that range.

For glacial melt, we assume the dFe going into the water in the ice shelf cavity is 29 nM (see **Methods**). Because much of the glacial meltwater comes out of the ice shelf cavity at depth, we will assume that the meltwater that makes it up into the euphotic zone gets mixed over a vertical range of 150–300 m over the open continental shelf. The estimated mean basal melt of the Ross Ice Shelf is 33-95 km^3 yr^{-1}, and the estimated residence time in the ice shelf cavity is 4–7 yr [*Loose et al.*, 2009; *Smethie and Jacobs*, 2005]. Using an area for the continental shelf of 4.2 x 10^5 km^2, the annual contribution of dFe from glacial melt into the euphotic zone would be 0.9–10.9 pM. The model-based estimate of 6.9 pM falls within this range, consistent with a minor contribution to the supply of dFe to the continental shelf.

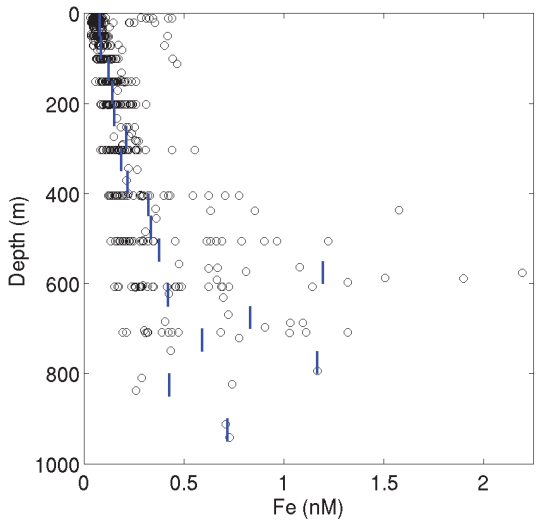

Figure S11. Composite profile of dFe measurements. Blue bars indicate the mean iron concentration for each 50 m depth bin.

References

Archer, D. E., and K. Johnson (2000), A model of the iron cycle in the ocean, *Global Biogeochemical Cycles*, *14*(1), 269-279.

Asper, V. L., and W. O. Smith, Jr. (1999), Particle fluxes during austral spring and summer in the southern Ross Sea, Antarctica, *Journal of Geophysical Research*, *104*(C3), 5345-5359.

Boyd, P. W., and M. J. Ellwood (2010), The biogeochemical cycle of iron in the ocean, *Nature Geosci*, *3*(10), 675-682.

Budgell, W. P. (2005), Numerical simulation of ice-ocean variability in the Barents Sea region: Towards dynamical downscaling, *Ocean Dynamics*.

Carter, S. P., and H. A. Fricker (2012), The supply of subglacial meltwater to the grounding line of the Siple Coast, West Antarctica, *Annals of Glaciology*, *53*(60), 267-280.

Cochlan, W. P., and D. A. Bronk (2001), Nitrogen uptake kinetics in the Ross Sea, Antarctica, *Deep-Sea Research II*, *48*(19–20), 4127-4153.

Comiso, J. C., R. Kwok, S. Martin, and A. L. Gordon (2011), Variability and trends in sea ice extent and ice production in the Ross Sea, *Journal of Geophysical Research: Oceans*, *116*(C4), C04021.

Death, R., J. L. Wadham, F. Monteiro, A. M. L. Brocq, M. Tranter, A. Ridgwell, S. Dutkiewicz, and R. Raiswell (2014), Antarctic ice sheet fertilises the Southern Ocean, *Biogeosciences*, *11*, 2635-2643.

Dinniman, M. S., J. M. Klinck, and W. O. Smith, Jr. (2011), A model study of Circumpolar Deep Water on the West Antarctic Peninsula and Ross Sea continental shelves, *Deep-Sea Research II*, *58*(13–16), 1508-1523.

Fragoso, G. M., and W. O. Smith, Jr. (2012), Influence of hydrography on phytoplankton distribution in the Amundsen and Ross Seas, Antarctica, *Journal of Marine Systems*, *89*, 19-29.

Jacobs, S. S., H. H. Hellmer, C. S. M. Doake, A. Jenkins, and R. M. Frolich (1992), Melting of ice shelves and the mass balance of Antarctica, *Journal of Glaciology*, *38*, 375-387.

Jeffries, M. O., and U. Adolphs (1997), Early winter ice and snow thickness distribution, ice structure and development of the western Ross Sea pack ice between the ice edge and the Ross Ice Shelf, *Antarctic Science*, *9*, 188-200.

Johnson, K. S., R. M. Gordon, and K. H. Coale (1997), What controls dissolved iron concentrations in the world ocean?, *Marine Chemistry*, *57*(3–4), 137-161.

Kohut, J., E. Hunter, and B. Huber (2013), Small-scale variability of the cross-shelf flow over the outer shelf of the Ross Sea, *Journal of Geophysical Research: Oceans*, *118*(4), 1863-1876.

Kwok, R. (2005), Ross Sea Ice Motion, Area Flux, and Deformation, *Journal of Climate*, *18*(18), 3759-3776.

Lingle, C. S., D. H. Schilling, J. L. Fastook, W. S. B. Paterson, and T. J. Brown (1991), A flow band model of the Ross Ice Shelf, Antarctica: Response to CO_2-induced climatic warming, *Journal of Geophysical Research: Solid Earth*, *96*(B4), 6849-6871.

Loose, B., P. Schlosser, W. M. Smethie, and S. Jacobs (2009), An optimized estimate of glacial melt from the Ross Ice Shelf using noble gases, stable isotopes, and CFC transient tracers, *Journal of Geophysical Research: Oceans*, *114*(C8), C08007.

Moore, J. K., and O. Braucher (2008), Sedimentary and mineral dust sources of dissolved iron to the world ocean, *Biogeosciences*, *5*, 631-656.

Nelson, D. M., and W. O. Smith, Jr. (1986), Phytoplankton bloom dynamics of the western Ross Sea ice edge—II. Mesoscale cycling of nitrogen and silicon, *Deep-Sea Research*, *33*(10), 1389-1412.

Padman, L., H. A. Fricker, R. Coleman, S. Howard, and L. Erofeeva (2002), A new tide model for the Antarctic ice shelves and seas, *Annals of Glaciology*, *34*, 247-254.

Parekh, P., M. J. Follows, and E. Boyle (2004), Modeling the global ocean iron cycle, *Global Biogeochemical Cycles*, *18*(1), GB1002.

Rignot, E., S. Jacobs, J. Mouginot, and B. Scheuchl (2013), Ice-Shelf Melting Around Antarctica, *Science*, *341*(6143), 266-270.

Sedwick, P. N., et al. (2011), Early season depletion of dissolved iron in the Ross Sea polynya: Implications for iron dynamics on the Antarctic continental shelf, *Journal of Geophysical Research*, *116*(C12), C12019.

Shabtaie, S., and C. R. Bentley (1987), West Antarctic ice streams draining into the Ross Ice Shelf: Configuration and mass balance, *Journal of Geophysical Research: Solid Earth*, *92*(B2), 1311-1336.

Smethie, W. M., and S. S. Jacobs (2005), Circulation and melting under the Ross Ice Shelf: estimates from evolving CFC, salinity and temperature fields in the Ross Sea, *Deep-Sea Research I*, *52*, 959-978.

Stern, A. A., M. S. Dinniman, V. Zagorodnov, S. W. Tyler, and D. M. Holland (2013), Intrusion of warm surface water beneath the McMurdo Ice Shelf, Antarctica, *Journal of Geophysical Research: Oceans*.

Willmott, C. J. (1981), On the evaluation of models, *Phys. Geogr.*, *2*, 184-194.